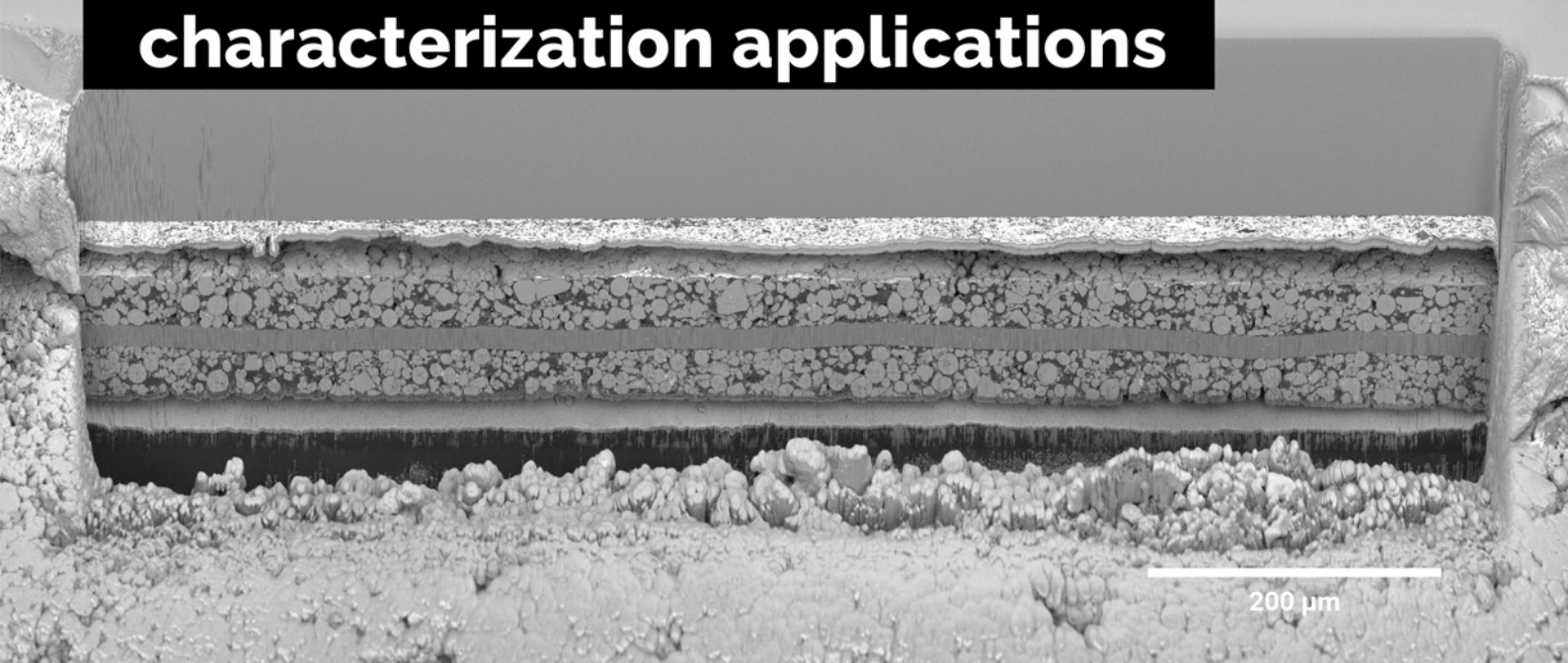


# A unique combination of Plasma FIB and field-free UHR SEM for the widest range of multiscale materials characterization applications



1 mm cross-section through a Li-ion battery electrode

## TESCAN AMBER X

- ✓ High throughput, large area FIB milling up to 1 mm
- ✓ Ga-free microsample preparation
- ✓ Ultra-high resolution, field-free FE-SEM imaging and analysis
- ✓ In-column SE and BSE detection
- ✓ Spot optimization for high-throughput, multi-modal FIB-SEM tomography
- ✓ Superior field of view for easy navigation
- ✓ Essence™ easy-to-use, modular graphical user interface



For more information visit

[www.tescan.com](http://www.tescan.com)

# Difluorobenzene-Based Locally Concentrated Ionic Liquid Electrolyte Enabling Stable Cycling of Lithium Metal Batteries with Nickel-Rich Cathode

Xu Liu, Alessandro Mariani, Thomas Diemant, Maria Enrica Di Pietro, Xu Dong, Matthias Kuenzel, Andrea Mele, and Stefano Passerini\*

Lithium metal batteries (LMBs) with nickel-rich cathodes are promising candidates for next-generation, high-energy batteries. However, the highly reactive electrodes usually exhibit poor interfacial compatibility with conventional electrolytes, leading to limited cyclability. Herein, a locally concentrated ionic liquid electrolyte (LCILE) consisting of lithium bis(fluorosulfonyl)imide (LiFSI), 1-ethyl-3-methylimidazolium bis(fluorosulfonyl)imide (EmimFSI), and 1,2-difluorobenzene (dFBn) is designed to overcome this challenge. As a cosolvent, dFBn not only promotes the  $\text{Li}^+$  transport with respect to the electrolyte based on the ionic liquid only, but also has beneficial effects on the electrode/electrolyte interphases (EIs) on lithium metal anodes (LMAs) and  $\text{LiNi}_{0.8}\text{Mn}_{0.1}\text{Co}_{0.1}\text{O}_2$  (NMC811) cathodes. As a result, the developed LCILE enables dendrite-free cycling of LMAs with a coulombic efficiency (CE) up to 99.57% at  $0.5 \text{ mA cm}^{-2}$  and highly stable cycling of Li/NMC811 cells (4.4 V) at C/3 charge and 1 C discharge ( $1 \text{ C} = 2 \text{ mA cm}^{-2}$ ) for 500 cycles with a capacity retention of 93%. In contrast, the dFBn-free electrolyte achieves lithium stripping/plating CE, and the Li/NMC811 cells' capacity retention of only 98.22% and 16%, respectively under the same conditions. The insight into the coordination structure, promoted  $\text{Li}^+$  transport, and EEI characteristics gives fundamental information essential for further developing (IL-based) electrolytes for long-life, high-energy LMBs.

the high reactivity of both the lithium metal anode (LMA) and Ni-rich NMC usually leads to poor interfacial compatibility with the conventional electrolytes and consequently limited cyclability.<sup>[4–7]</sup> Without a sufficiently protective solid–electrolyte interphase (SEI) on LMAs, side reactions between lithium and electrolytes cause lithium dendritic growth and low stripping/plating coulombic efficiency (CE).<sup>[8–10]</sup> At the cathode/electrolyte interface, parasitic electrolyte degradation occurs due to the highly reactive  $\text{Ni}^{4+}$  species generated upon delithiation. This is accelerated by increasing Ni content in the cathode, resulting in limited reversibility of the Ni-rich NMC cathode and thickening of the cathode/electrolyte interphase (CEI) upon cycling.<sup>[11,12]</sup> Among the strategies proposed to enhance the cyclability of LMBs, electrolyte engineering appears to be one of the most effective and feasible approaches, as the electrolyte plays a key role in the CEI and SEI formation.<sup>[13–19]</sup>

Ionic liquid electrolytes (ILEs), with high electrochemical stability, are valuable options for Li/Ni-rich NMC cells in this context.<sup>[20–23]</sup> For instance,

Wu et al.<sup>[24]</sup> have recently reported highly stable cycling of Li/LiNi<sub>0.88</sub>Co<sub>0.09</sub>Mn<sub>0.03</sub>O<sub>2</sub> cells up to 300 cycles with a capacity retention of 88% in [LiTFSI]<sub>0.2</sub>[Pyr<sub>14</sub>FSI]<sub>0.8</sub> (LiTFSI = lithium bis(trifluoromethanesulfonyl)imide, Pyr<sub>14</sub>FSI = N-butyl-N-methylpyrrolidinium bis(fluorosulfonyl)imide). Unfortunately, the excellent performance has been only achieved with low cathode mass loading (<5 mg cm<sup>-2</sup>), or/and low current density

## 1. Introduction

Lithium metal batteries (LMBs) are considered to be a promising candidate for the next-generation high-energy-density rechargeable batteries,<sup>[1]</sup> particularly when high-capacity/high-voltage cathode materials, e.g., nickel (Ni)-rich  $\text{LiNi}_x\text{Mn}_y\text{Co}_{1-x-y}\text{O}_2$  (NMC,  $x \geq 0.6$ ),<sup>[2,3]</sup> are employed. However,

X. Liu, A. Mariani, T. Diemant, X. Dong, M. Kuenzel, S. Passerini  
Helmholtz Institute Ulm (HIU)  
Helmholtzstraße 11, D-89081 Ulm, Germany  
E-mail: stefano.passerini@kit.edu

 The ORCID identification number(s) for the author(s) of this article can be found under <https://doi.org/10.1002/aenm.202200862>.

© 2022 The Authors. Advanced Energy Materials published by Wiley-VCH GmbH. This is an open access article under the terms of the Creative Commons Attribution License, which permits use, distribution and reproduction in any medium, provided the original work is properly cited.

X. Liu, A. Mariani, T. Diemant, X. Dong, M. Kuenzel, S. Passerini  
Karlsruhe Institute of Technology (KIT)  
P.O. Box 3640, D-76021 Karlsruhe, Germany

M. E. D. Pietro, A. Mele  
Politecnico di Milano  
Materials and Chemical Engineering “Giulio Natta”  
Department of Chemistry  
Piazza Leonardo da Vinci 32, Milan I-20133, Italy

DOI: 10.1002/aenm.202200862

**Table 1.** Compositions of the electrolytes.

Electrolyte	Composition	Molar ratio	Mass ratio	Density [20 °C] [g cm <sup>-3</sup> ] <sup>-1</sup>	Li <sup>+</sup> molarity [20 °C] [mol L <sup>-1</sup> ] <sup>-1</sup>
FE	LiFSI:EmimFSI	1:2	0.243:0.757	1.5558	2.02
FEdF	LiFSI:EmimFSI: dFBn	1:2:2	0.187:0.584:0.229	1.4616	1.46

( $\leq 0.3$  mA cm<sup>-2</sup>).<sup>[24]</sup> In fact, the high viscosity and sluggish Li<sup>+</sup> transport of ILEs at room temperature make it difficult to gain similar performance with high-mass-loading cathodes and at high current densities.<sup>[21,24]</sup>

Introducing low-viscosity cosolvents to ILEs has been proven as a feasible route to reduce viscosity and promote Li<sup>+</sup> transport.<sup>[25–28]</sup> On the other hand, the cosolvent also affects the electrolyte/electrode interfacial stability. The early adopted cosolvents (e.g., carbonate esters), strongly coordinating to Li<sup>+</sup> and interrupting the Li<sup>+</sup>-anions solvation, are unstable toward LMAs, leading to unstable SEIs and low lithium plating/stripping CEs.<sup>[29,30]</sup> In recent years, nonsolvating hydrofluoroethers (HFEs) have been proposed as a new class of cosolvents for ILEs,<sup>[29–32]</sup> which is inspired by a similar approach applied to organic-solvent-based concentrated electrolytes.<sup>[33–39]</sup> Due to the poor solvation capability of HFEs toward Li<sup>+</sup>, the ILEs, needing a high Li<sup>+</sup> concentration to unlock non-vehicular Li<sup>+</sup> transport,<sup>[40,41]</sup> are diluted, but with the local Li<sup>+</sup> coordination preserved. This, and HFEs' high compatibility toward LMAs, promote Li<sup>+</sup> transport in ILEs without compromising the CE of Li stripping/plating.<sup>[29–32]</sup> The ILEs diluted with nonsolvating cosolvent are usually named locally concentrated ionic liquid electrolytes (LCILEs).

The rational design, including the organic cation,<sup>[32]</sup> anion,<sup>[30]</sup> and components' concentrations,<sup>[29–31]</sup> of HFE-based LCILEs allows fast charge/discharge (up to 2 mA cm<sup>-2</sup>) and high lithium stripping/plating CE (up to 99%), resulting in ILEs stepping further on their road to practical application. Nonetheless, the cyclability of high-voltage LMAs employing HFE-based LCILEs is still unsatisfactory under the conditions of high cathode mass loadings and/or high current densities, particularly for those employing NMC cathodes.<sup>[29–32]</sup> Therefore, the development of new cosolvents that can further strengthen the EEIs, especially the CEI, in the LCILEs is still demanded. Not long ago, fluorinated aromatic compounds (FACs), e.g., 1,2-difluorobenzene (dFBn), with lower affinity to Li<sup>+</sup> and stronger F-donating power than HEFs have been demonstrated as a better choice for ether and carbonate-based concentrated electrolytes.<sup>[42–44]</sup> To the best of our knowledge, though, LCILEs with FAC cosolvents have not been studied yet.

Herein, a FAC-based LCILE, i.e., [LiFSI]<sub>1</sub>[EmimFSI]<sub>2</sub>[dFBn]<sub>2</sub> (FEdF), is reported featuring lithium stripping/plating CEs up to 99.57% at 0.5 mA cm<sup>-2</sup> and highly stable cycling of Li/NMC811 cells (4.4 V) at high current (C/3 charge, 1C discharge, 1C = 2 mA cm<sup>-2</sup>) for 500 cycles with a remarkable capacity retention of 93%. To reveal the role of the dFBn cosolvent, a comparative study of FEdF and the cosolvent-free ILE, i.e., [LiFSI]<sub>1</sub>[EmimFSI]<sub>2</sub> (FE), in terms of their physicochemical properties, solution structure, electrochemical performance, and the interphase chemistry, has been conducted. The chemical sketches of the components are shown in Figure S1 (Supporting Information).

## 2. Results and Discussion

### 2.1. Physicochemical Properties and Solvation Structure

The formulation, density, and Li<sup>+</sup> concentration of FE and FEdF are displayed in **Table 1**. The physicochemical properties of the electrolytes at 20 °C have been measured. As shown in **Figure 1a,b**, the addition of dFBn to FE leads to a decrease in the viscosity from 67.5 to 24.7 mPa s and an increase in ionic conductivity from 5.28 to 8.84 mS cm<sup>-1</sup>, indicating improved electrolyte fluidity and ionic mobility. Since all the ionic carriers contribute to the ionic conductivity while only Li<sup>+</sup> ions account for the operation of the LMAs, pulsed field gradient (PFG) NMR was performed to measure the self-diffusion coefficients of all ionic charge carriers, i.e., Li<sup>+</sup>, Emim<sup>+</sup>, and FSI<sup>-</sup>, in the electrolytes. As summarized in **Figure 1c**, all ionic species exhibit higher self-diffusion coefficients in FEdF than in FE. Specifically, the Li<sup>+</sup> self-diffusion coefficient in FEdF is 2.5 times of that in FE, proving the enhanced translational mobility of Li<sup>+</sup>.

In addition to the Li<sup>+</sup> mobility, the Li<sup>+</sup> concentration and the mobility of other ions also affect the Li<sup>+</sup> transport ability of the electrolytes, according to the classical diffusion model described by the Sand equation:<sup>[45]</sup>

$$\tau = \pi D_{\text{Li}} \left( \frac{eC_0}{2J(1-t_{\text{Li}^+})} \right)^2 \quad (1)$$

here,  $\tau$ , the Sand time, describes the time at which the Li<sup>+</sup> concentration goes to zero at the negative electrode;  $J$  is the applied current density;  $D_{\text{Li}}$ ,  $C_0$ , and  $t_{\text{Li}^+}$  are the self-diffusion coefficient, initial concentration, and transference number of Li<sup>+</sup>.  $C_0$  and  $D_{\text{Li}}$  of FE and FEdF are shown in **Table 1** and **Figure 1c**, respectively. The apparent Li<sup>+</sup> transference numbers ( $t_{\text{Li}^+}$ ) can be calculated with the self-diffusion coefficients ( $D_i$ ) of the ionic species  $i$  according to the following equation:

$$t_{\text{Li}^+} = \frac{D_{\text{Li}}x_{\text{Li}}}{D_{\text{Li}}x_{\text{Li}} + D_{\text{FSI}}x_{\text{FSI}} + D_{\text{Emim}}x_{\text{Emim}}} \quad (2)$$

where  $x_i$  denotes the mole fraction of the ionic species  $i$ . For both FE and FEdF,  $x_{\text{Li}}$ ,  $x_{\text{FSI}}$ , and  $x_{\text{Emim}}$  are 1/6, 2/6, and 3/6, respectively. The calculated  $t_{\text{Li}^+}$  in FE and FEdF are 0.134 and 0.120, respectively, which is identical to the previously reported values of ILEs.<sup>[30,32]</sup> The slightly decreased value with the addition of dFBn can be ascribed to the more pronounced increase of  $D_{\text{Emim}}$  than that of  $D_{\text{Li}}$ .

Applying the obtained self-diffusion coefficient, initial concentration, and transference number of Li<sup>+</sup> to the Sand equation (Equation 1), one can find that the Sand time in FEdF is 1.267 times of that in FE at the same current density ( $J$ ),

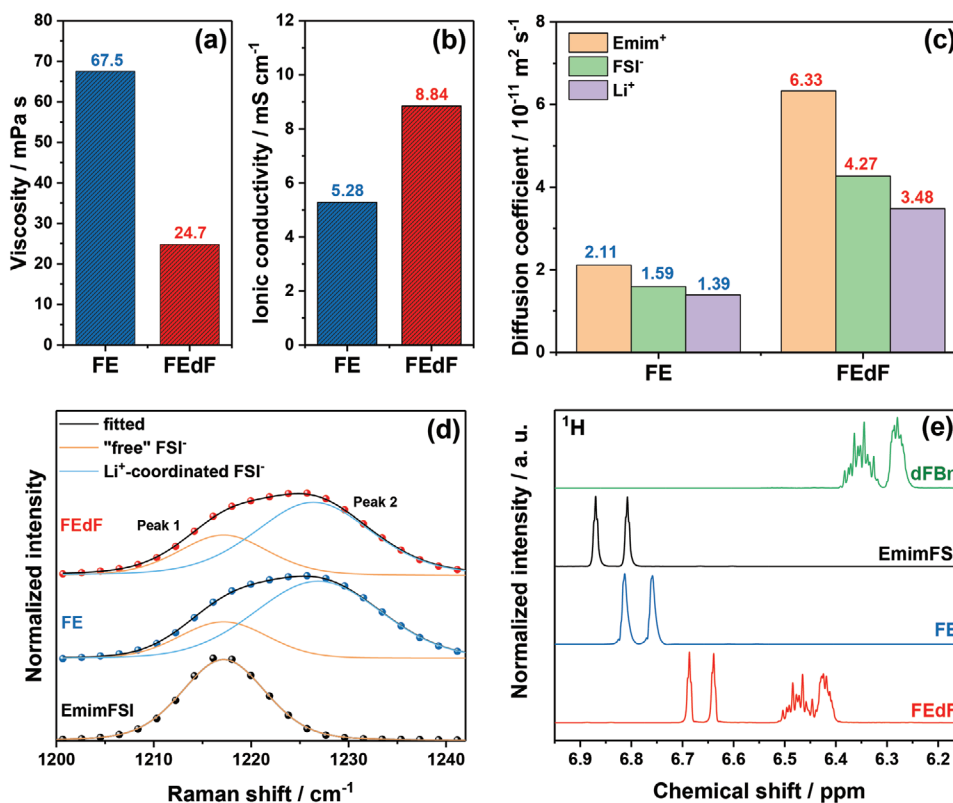


**Figure 1.** Physicochemical characterization of the FE and FEdF electrolytes at 20 °C. a) Viscosities and b) ionic conductivities. c) Self-diffusion coefficients of the ions in the electrolytes measured via PFG-NMR. d) Raman spectra. The “free” FSI<sup>−</sup> means the FSI<sup>−</sup> weakly coordinating to Emim<sup>+</sup>. e) 1D <sup>1</sup>H NMR spectra in the region 6.1–7.0 ppm.

demonstrating the promoted Li<sup>+</sup> transport ability. Since FEdF exhibits lower Li<sup>+</sup> concentration and Li<sup>+</sup> transference number with respect to FE, the superior Li<sup>+</sup> transport ability of FEdF mainly comes from its high self-diffusion coefficient of Li<sup>+</sup>.

The diffusion coefficient of Li<sup>+</sup> ( $D_{\text{Li}}$ ) is correlated to the viscosity ( $\eta$ ) of the liquid and the hydrodynamic radius of Li<sup>+</sup> ( $r_{\text{Li}}$ ), as described by the Stokes-Einstein equation:<sup>[46]</sup>

$$D_{\text{Li}} = \frac{k_{\text{B}}T}{6\pi\eta r_{\text{Li}}} \quad (3)$$

where  $k_{\text{B}}$  is the Boltzmann constant and  $T$  is the temperature (293 K). Interestingly, the ratio of  $D_{\text{Li}}$  in FEdF and FE is very close to the ratio of  $1/\eta$  for FEdF and FE (2.5 vs 2.7, respectively), which points to a very similar hydrodynamic radius of Li<sup>+</sup> in these two electrolytes. As the hydrodynamic radius is closely related to the local solvation environment, one can further infer that the local coordination of Li<sup>+</sup> is similar in FE and FEdF, i.e., the addition of dFBn does not significantly affect the solvation of Li<sup>+</sup>.

Raman spectra of FE and FEdF were recorded to check the coordination between Li<sup>+</sup> and FSI<sup>−</sup> in more detail. The region reflecting the  $\nu_{\text{s}}(\text{SO}_2)$  mode of FSI<sup>−</sup> is shown in Figure 1d. The peak (Peak 1) located  $\approx 1217 \text{ cm}^{-1}$  in the spectrum of EmimFSI is associated with “free” FSI<sup>−</sup> only weakly coordinated with Emim<sup>+</sup>.<sup>[47]</sup> The addition of LiFSI leads to the presence of a new peak  $\approx 1227 \text{ cm}^{-1}$  (Peak 2), which is ascribed to the FSI<sup>−</sup>

coordinating to Li<sup>+</sup>. The spectrum of FEdF does not show significant changes with respect to that of FE. The fraction ( $f$ ) of FSI<sup>−</sup> coordinated by Li<sup>+</sup> in these two solutions have been further calculated via Equation 4:

$$f = \frac{A_2}{A_1 + A_2} \quad (4)$$

where  $A_1$  and  $A_2$  are the areas of peaks 1 and 2, respectively. The  $f$  in FE and FEdF was calculated to be 75% and 70%, respectively, confirming that the addition of dFBn indeed does not substantially affect the coordination between Li<sup>+</sup> and FSI<sup>−</sup>. The  $\nu_{\text{s}}(\text{SNS})$  mode of FSI<sup>−</sup> in the region of 680–800  $\text{cm}^{-1}$  was also checked (Figure S2, Supporting Information),<sup>[47]</sup> but the signals overlap with those of Emim<sup>+</sup> and dFBn, which makes the further analysis difficult.

Apart from the Li<sup>+</sup>-FSI<sup>−</sup> coordination, the chemical environment of Emim<sup>+</sup> and dFBn in the electrolytes was also explored via <sup>1</sup>H NMR spectroscopy. As shown in Figure 1e, the addition of LiFSI to EmimFSI leads to the upfield shift of the peaks located at 6.87 and 6.81 ppm, corresponding to the N–CH = CH–N protons of the imidazolium ring, to 6.81 and 6.76 ppm, respectively. This can be attributed to lower coordination of Emim<sup>+</sup> to FSI<sup>−</sup> as evidenced in Figure 1d. With the addition of dFBn to FE, these two peaks shift to even lower frequencies. Meanwhile, the aromatic peaks from dFBn shift from the region of 6.25–6.40 ppm in the spectrum of dFBn to 6.40–6.55 ppm

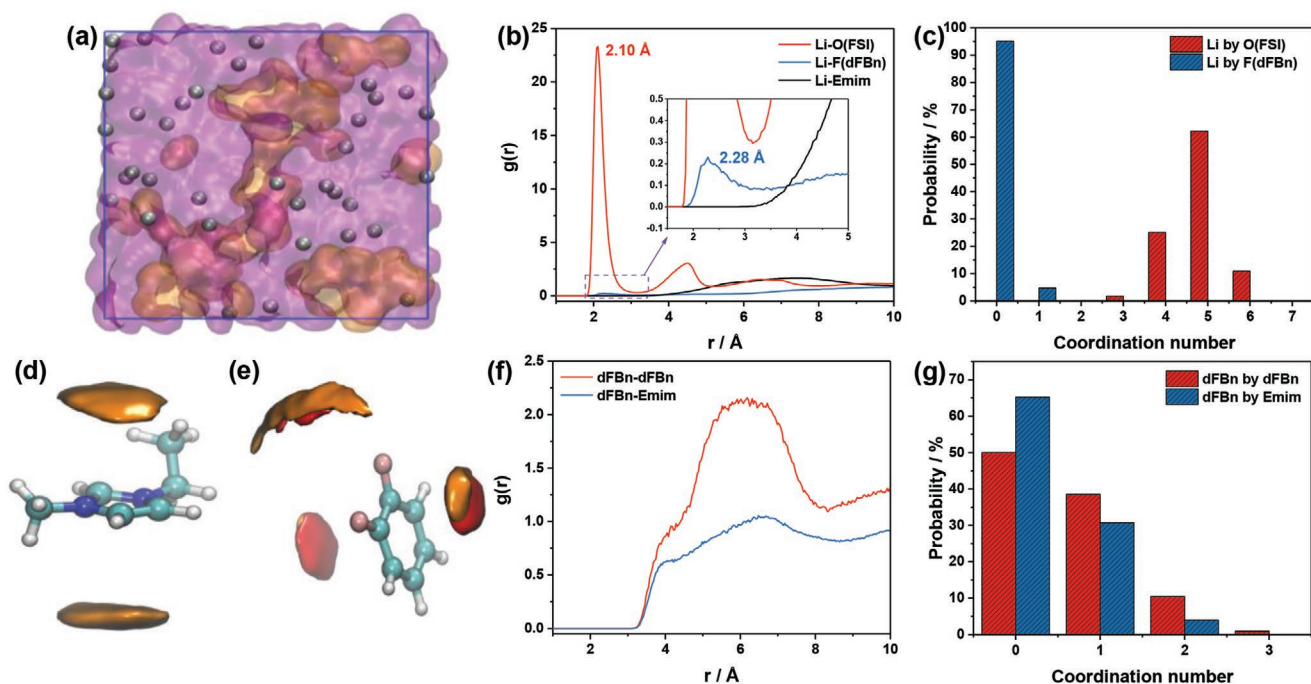


**Figure 2.** MD simulation for FEdF. a) Snapshot of the MD simulated box. The grey spheres, orange clouds, and purple clouds represent  $\text{Li}^+$ , dFBn, and  $\text{Emim}^+/\text{FSI}^-$ , respectively. b) Radial distribution functions (RDFs) of Li-O(FSI), Li-F(dFBn), and Li-Emim pairs. c) Coordination number populations of Li by O(FSI) and F(dFBn). Spatial distribution functions around the centers of d)  $\text{Emim}^+$  and e) dFBn, respectively. The yellow and red clouds represent the dFBn and  $\text{Emim}^+$ , respectively. f) RDFs of dFBn-dFBn and dFBn-Emim pairs. g) Coordination number populations of dFBn by dFBn and Emim.

for FEdF. These results reveal that there is some coordination related to  $\text{Emim}^+$  or/and dFBn in FEdF.

To elucidate the solution structure in FEdF, molecular dynamics simulations were carried out. Figure 2a shows a snapshot of FEdF, in which the grey spheres, orange clouds, and purple clouds represent  $\text{Li}^+$ , dFBn, and  $\text{Emim}^+/\text{FSI}^-$ , respectively. Most  $\text{Li}^+$  ions are embedded in the domains of  $\text{Emim}^+/\text{FSI}^-$  and are not exposed to dFBn, which suggests a rather limited interaction between  $\text{Li}^+$  and dFBn. The solvation of  $\text{Li}^+$  is further characterized via radial distribution functions (RDF), as shown in Figure 2b. The profiles of Li-O(FSI), Li-F(dFBn), and Li-Emim represent the interaction between  $\text{Li}^+$  and oxygen from FSI $^-$ , fluorine from dFBn, and the geometric center of the Emim ring, respectively. A sharp peak at 2.10 Å in the Li-O(FSI) curve is observed, while the Li-Emim curve only displays a negligible intensity in the region below 3.5 Å. This result indicates that the  $\text{Li}^+$  ions embedded in the  $\text{Emim}^+/\text{FSI}^-$  domain, as expected, coordinate with FSI $^-$  rather than  $\text{Emim}^+$ . Besides, a small peak at 2.28 Å is observed in the Li-F(dFBn) curve, pointing to the presence of some fluorine atoms of dFBn in the primary  $\text{Li}^+$  solvation sheath. To quantify the coordination of FSI $^-$  and dFBn to  $\text{Li}^+$ , the  $\text{Li}^+$  coordination number population was extracted and is shown in Figure 2c. The probability for a  $\text{Li}^+$  not to be coordinated by fluorine atoms from dFBn is 95%, while the probability of being coordinated by at least four oxygen from FSI $^-$  is higher than 98%. The average number of fluorine atoms from dFBn or oxygen atoms from FSI $^-$  coordinating to each  $\text{Li}^+$  was calculated to be 0.05 and 4.82, respectively. Therefore, the co-ordination of dFBn to  $\text{Li}^+$  can be neglected with respect to that of FSI $^-$  to  $\text{Li}^+$ .

To check the coordination of  $\text{Emim}^+$  and dFBn, the spatial distribution functions around the centers of their rings are shown in Figure 2d,e, respectively. The iso-surfaces for a density of 150% of the bulk average density are displayed. The orange and red surfaces represent the geometrical centres of dFBn and  $\text{Emim}^+$  rings, respectively. As shown in Figure 2d, the orange distribution clouds facing the aromatic ring of  $\text{Emim}^+$  demonstrate the interaction between  $\text{Emim}^+$  and dFBn. Since the positively charged five-membered ring of  $\text{Emim}^+$  obeys the Hückel rule,  $\text{Emim}^+$  is conjugated. It could transfer part of its positive charge to aromatic dFBn via  $\pi$ - $\pi$  stacking as observed in Figure 2d, which is also responsible for the change of the chemical shift of  $\text{Emim}^+$  and dFBn in the  $^1\text{H}$  NMR spectra (Figure 1e). A similar distribution of  $\text{Emim}^+$  around central dFBn is also seen in Figure 2e, despite a competition between dFBn and  $\text{Emim}^+$  for the first shell. Besides, an equatorial correlation on the fluorinated side also appears, highlighting the shift from a prominent  $\pi$ - $\pi$  interaction to a dipole-dipole correlation due to the electron withdrawing effect of fluorine. The presence of the  $\pi$ - $\pi$  interaction is also evidenced via RDFs of dFBn (Figure 2f). The competition between  $\text{Emim}^+$  and dFBn for the first shell is more clearly seen from the corresponding coordination number population shown in Figure 2g. The average number of dFBn and  $\text{Emim}^+$  coordinates to each dFBn was calculated to be 0.62 and 0.39.

Taken together, these results clearly prove that FEdF is a typical LCILE, thanks to the poor affinity of dFBn to  $\text{Li}^+$ , but an evident interaction with  $\text{Emim}^+$ . The former one leads to the preserved  $\text{Li}^+$  local solvation structure ( $\text{Li}^+/\text{FSI}^-$  solvation), while the latter guarantees the miscibility of FE and dFBn. The

promoted  $\text{Li}^+$  diffusion coefficient and  $\text{Li}^+$  transport ability upon addition of dFBn can be therefore attributed to the reduced viscosity and, at the same time, well-maintained local solvation structure of  $\text{Li}^+$ .

## 2.2. Electrochemical Performance of LMAs in the Electrolytes

The electrochemical performance of LMAs in the two electrolytes was first evaluated via Li/Li symmetric cells at 20 °C. The voltage profiles of Li/Li cells employing FE and FEdF as electrolytes at different current densities, but a constant areal capacity of 1 mAh  $\text{cm}^{-2}$  for each stripping/plating cycle are shown in Figure 3a. Both cells can sustain a current density of up to 3 mA  $\text{cm}^{-2}$ , but the FEdF-based cell exhibits much lower polarization and flatter voltage plateaus (Figure S3, Supporting Information) than the FE-based cell. The average voltage plateaus of the cells upon charge processes at increasing current densities are summarized in Figure 3b. At the same current density, the value for the FEdF-based cell is only half of that for the FE-based cell, which is associated with the superior  $\text{Li}^+$  transport in FEdF. In addition, it is worth mentioning that the voltage plateaus of the cell employing FEdF are only 64 and 86 mV at 2.0 and 3.0 mA  $\text{cm}^{-2}$ , respectively, which demonstrates the fast kinetics of LMAs in FEdF.

The Li/Li cells were then subjected to continuous galvanostatic cycling with a current density of 1 mA  $\text{cm}^{-2}$  and a cycling capacity of 1 mAh  $\text{cm}^{-2}$  to test the cyclability of LMAs in the electrolytes. The voltage profiles are displayed in Figure 3c. Without activation cycling at low current density, the cell employing FE shows high polarization and a short lifespan (lower than 100 h). In contrast, the cell with FEdF as the electrolyte operates for more than 800 h (400 cycles) with only a slight increase in the average voltage plateau from 38 mV at the 25th cycle to 61 mV at the 400th cycle. The voltage profiles at selected cycles are shown in Figure S4 (Supporting Information).

The improved cyclability of Li/Li cells implies an enhanced CE of lithium stripping/plating in the FEdF electrolytes. To verify this, the CE was evaluated via the cycling of lithium metal deposited on Cu.<sup>[48]</sup> Before cycling, one formation cycle was performed by plating 5 mAh  $\text{cm}^{-2}$  of Li on the Cu substrate and stripping the Li to 1 V. Subsequently, 5 mAh  $\text{cm}^{-2}$  Li was first deposited on the Cu electrode to grant a Li reservoir, followed by repeated Li stripping/plating at 1 mAh  $\text{cm}^{-2}$  for 11 cycles. Finally, the remaining Li metal after the 11 cycles was stripped to 1 V. The average CE can then be obtained by dividing the total stripping capacity by the total plating capacity after the initial formation cycle. The calculated results are summarized in Figure 3d; the voltage profiles of the Li/FEdF/Cu and Li/FE/Cu cells are shown in Figure 3e and Figure S5 (Supporting Information), respectively.

The CE in FE (98.22% and 97.56% at 0.5 and 1.0 mA  $\text{cm}^{-2}$ , respectively) is higher than that for conventional carbonate-based electrolytes, demonstrating the good compatibility of FE toward LMAs. Nonetheless, these values are still far from practical requirements. What is worse, the cells with 2 mA  $\text{cm}^{-2}$  suffered short-circuit, as shown in Figure S5c (Supporting Information). When FEdF was employed as the electrolyte, the CE significantly improved to 99.57% at 0.5 mA  $\text{cm}^{-2}$  and exhibited

only a slight decrease to 99.39% at 2.0 mA  $\text{cm}^{-2}$ , demonstrating the high reversibility of Li stripping/plating processes in FEdF. The 99.57% CE for Li plating/stripping at 0.5 mA  $\text{cm}^{-2}$  in FEdF is the highest value reported for LCILEs up to now,<sup>[29–32]</sup> and is comparable to the recorded value of other locally concentrated electrolytes based on phosphate (99.2%),<sup>[35]</sup> sulfone (98.8%),<sup>[49]</sup> ether (99.5%),<sup>[8]</sup> or carbonate ester (99.5%).<sup>[34]</sup>

## 2.3. Electrochemical Performance of Li/NMC811 Cells

To evaluate the compatibility of the electrolytes with a Ni-rich cathode, Li/NMC811 coin cells employing thick Li anodes (500  $\mu\text{m}$ ) and excess electrolyte (75  $\mu\text{L}$ ) were assembled and cycled in the voltage window of 2.8–4.4 V at 20 °C. The mass loading of the NMC811 was 10 mg  $\text{cm}^{-2}$ , and the positive current collector was Al foil. Although FSI<sup>-</sup> was employed, no recognizable anodic corrosion of the Al foil was observed within 2.8–4.4 V in the electrolytes, as shown in Figure S6 (Supporting Information).

As a first step, the influence of discharge rate on the capacity was assessed. After five formation cycles at C/10 (1C = 200 mA  $\text{g}^{-1}$  = 2 mA  $\text{cm}^{-2}$ ), the cells were cycled with an increasing discharge rate, but a constant charge rate of C/3. The discharge-specific capacities of the cells are summarized in Figure 4a. The dis-/charge profiles at selected rates are shown in Figures 4b and S7 (Supporting Information). In general, the capacity delivered in FEdF is higher than that in FE, but the gap is not wide at relatively low currents ( $\leq C/2$ ). For example, in the formation cycles (C/10), 208 and 201 mAh  $\text{g}^{-1}$  are obtained in FEdF and FE, respectively; at C/2 discharge, the specific capacity is 195 and 188 mAh  $\text{g}^{-1}$ , respectively. Nonetheless, when the discharge current is increased to 1C, the discharge specific capacity is only 144 mAh  $\text{g}^{-1}$  for the Li/FE/NMC811 cell, while the FEdF-based cell still exhibits 183 mAh  $\text{g}^{-1}$ . The superior rate capability of the Li/NMC811 cells employing FEdF clearly benefits from the promoted  $\text{Li}^+$  mobility in the electrolyte and the faster Li stripping/plating kinetics.

As it has been proven that the asymmetric faster discharge protocol can promote the cyclability of LMBs, the cyclability of the Li/NMC811 cells was further evaluated at C/3 charge and 1C discharge after two formation cycles at C/10.<sup>[50]</sup> The discharge specific capacity, as well as the CE, are summarized in Figure 4c. The dis-/charge profiles of selected cycles are shown in Figure 4d,e. Both cells show increasing capacity in the initial few tens of cycles, while the evolution of the capacity upon cycling is very different after that. The Li/FE/NMC811 cell shows a fast capacity fading from its peak capacity, i.e., 168 mAh  $\text{g}^{-1}$  at the 23rd cycle, to 49 mAh  $\text{g}^{-1}$  at the 250th cycle, and delivers only 27 mAh  $\text{g}^{-1}$  at the 450th cycle. In contrast, after reaching the peak capacity of 192 mAh  $\text{g}^{-1}$  around the 85th cycle, the cell employing FEdF shows stable cycling and delivers 179 mAh  $\text{g}^{-1}$  at the 500<sup>th</sup> cycle, which corresponds to a capacity retention of 93%. This remarkable cycling stability demonstrates the excellent compatibility of FEdF with the Ni-rich NMC811.

Since thick Li metal anodes and excess amount of electrolytes were used in both cells, the CE in the early cycling mainly reflects the reversibility of the NMC811 cathodes.<sup>[51]</sup> As shown in Figure 4c, the initial CE (ICE) of the cells employing FE

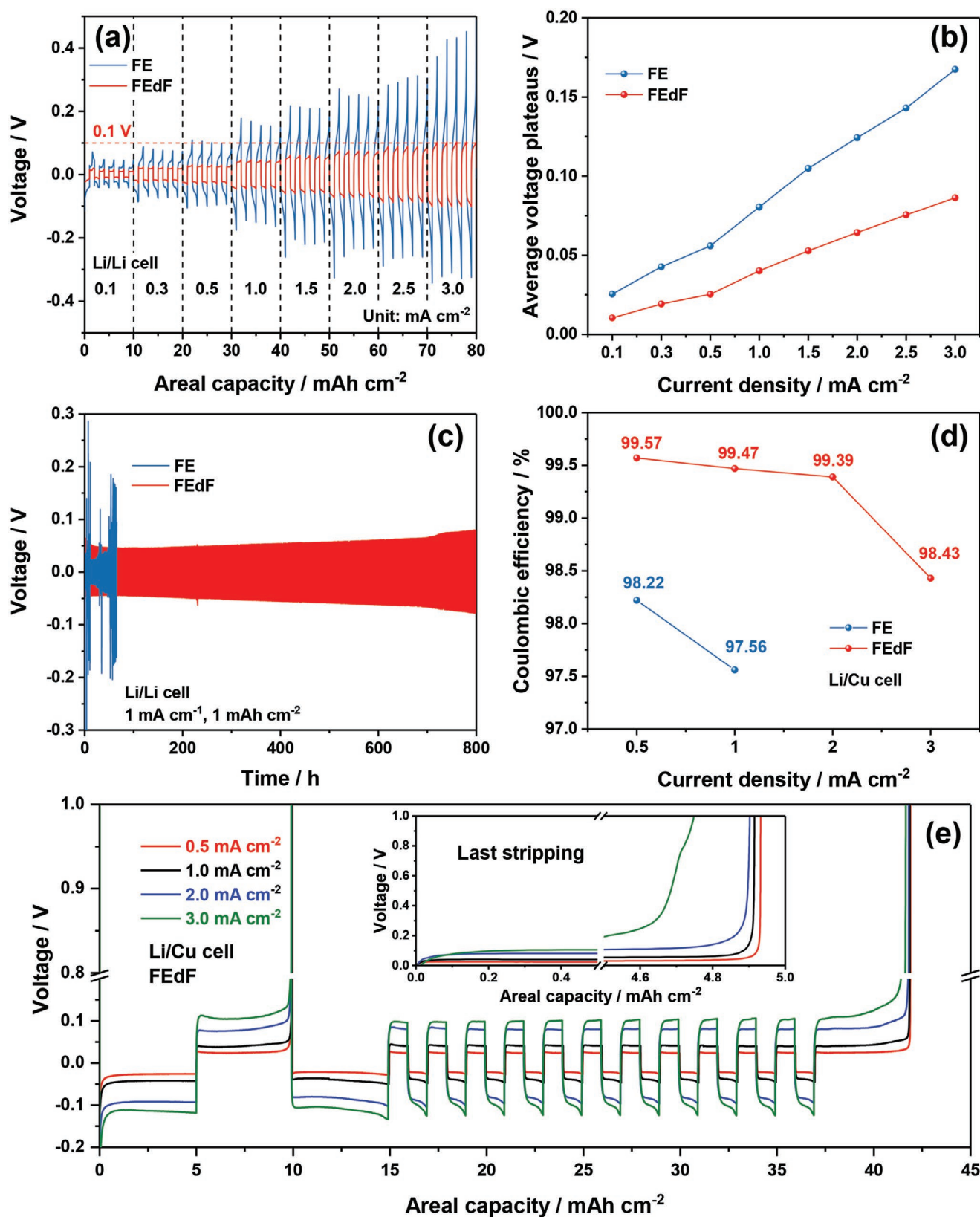


**Figure 3.** Electrochemical performance of LMAs in the two electrolytes. a) Voltage profiles and b) the average voltage plateaus of Li plating/stripping processes in Li/Li cells at various current densities. c) Long-term cycling voltage profiles for Li/Li cells. d) Li plating/stripping CE at various current densities. e) The voltage profile of Li/Cu cells for the evaluation of Li plating/stripping CE in FEdF. The inset shows the voltage profile of the last stripping process.

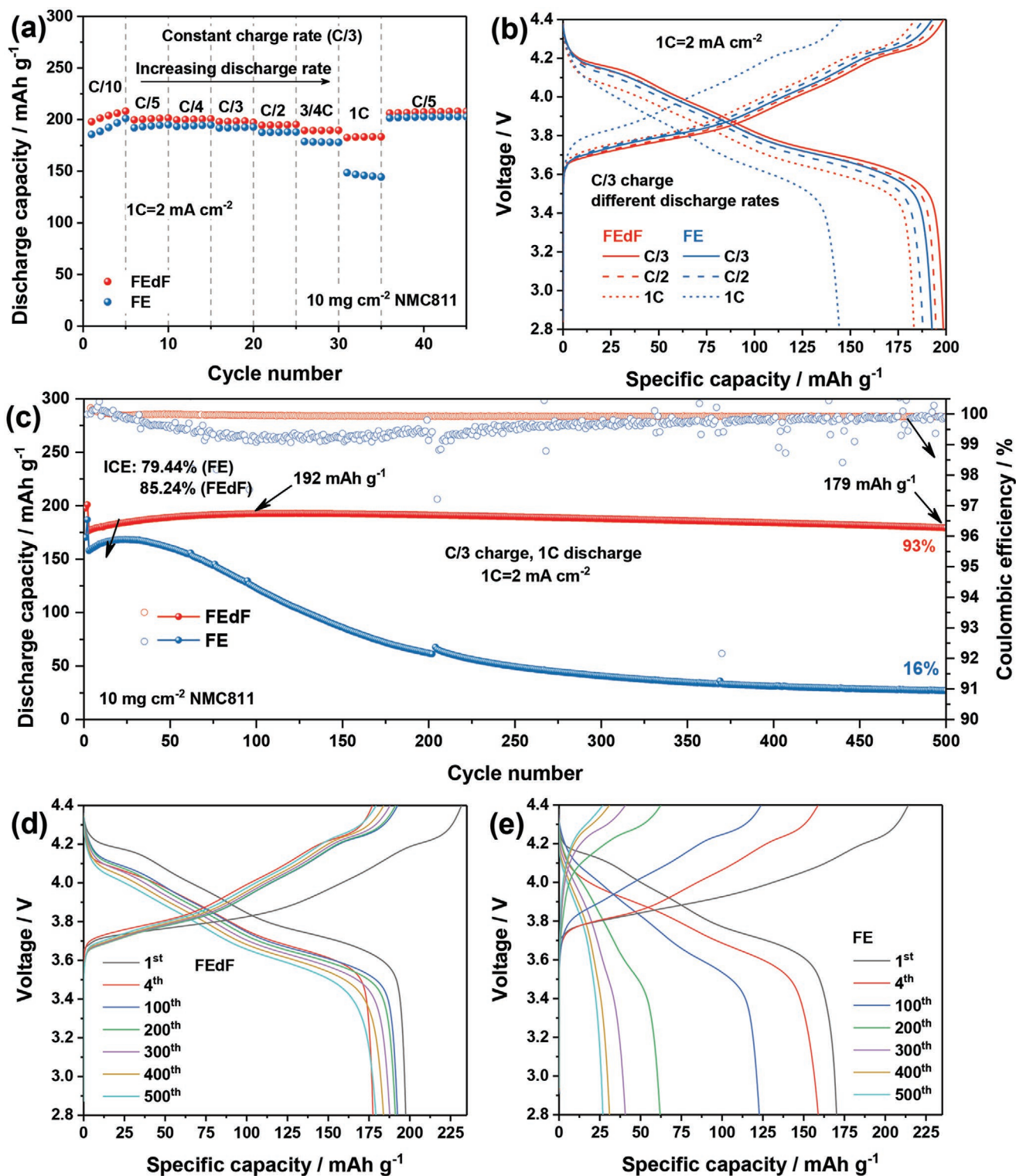


**Figure 4.** Performance of NMC811 (10 mg cm<sup>-2</sup>) in LMBs with thick LMAs (500 μm) and an excess amount of electrolyte (75 μL). a) Rate performance at different discharge C-rates with a constant charge rate of C/3 after five formation cycles at C/10. b) The dis-/charge profiles of the cells at selected C-rates. c) The evolution of discharge specific capacity and CE during long-term cycling of the cells at C/3 charge and 1C discharge after two formation cycles at C/10. The dis-/charge profiles of the cells employing d) FEdF and e) FE. 1C is 200 mA g<sup>-1</sup>, equaling 2 mA cm<sup>-2</sup>.

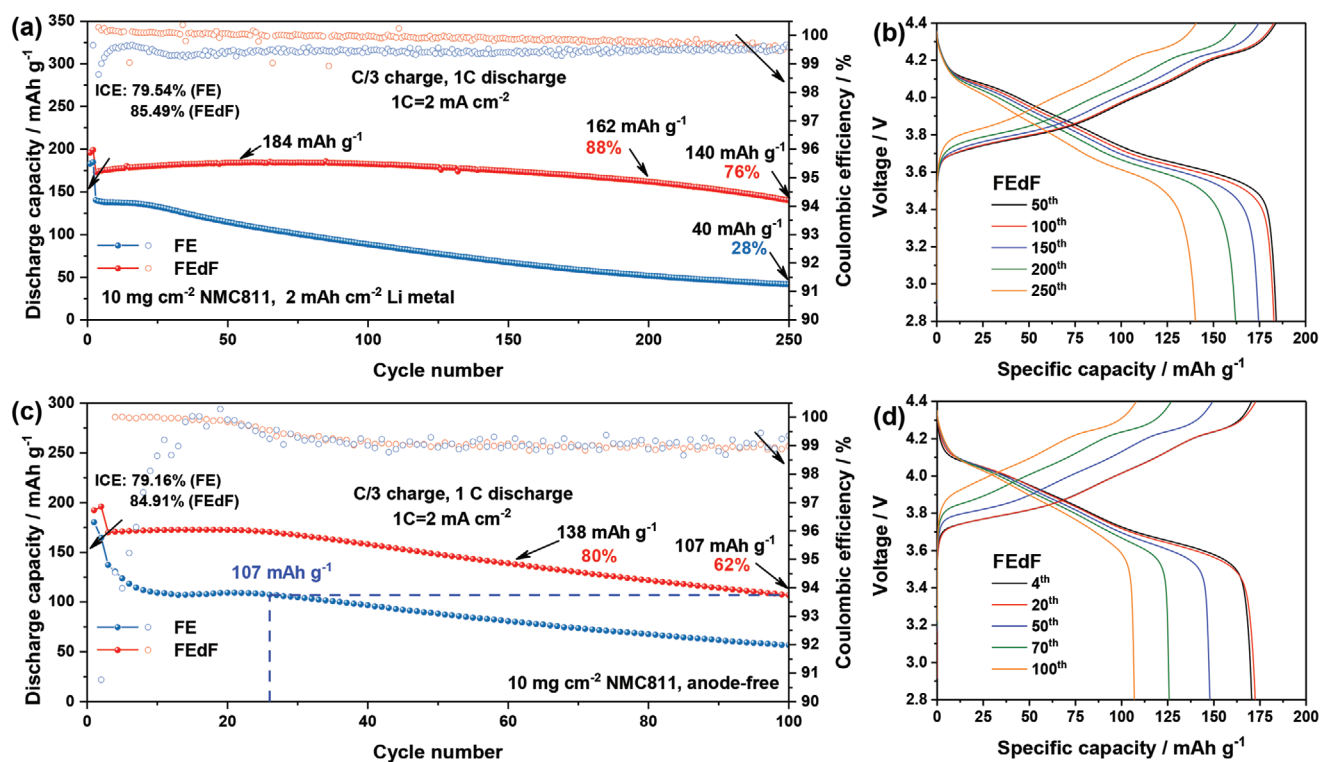


**Figure 5.** Cycling performance of NMC811 ( $10 \text{ mg cm}^{-2}$ ) in LMBs with thin LMAs and  $20 \mu\text{L}$  electrolyte in each cell. a) The evolution of discharge specific capacity and CE of the Li/NMC811 cells employing LMAs with an areal capacity of  $2 \text{ mAh cm}^{-2}$ . b) Dis-/charge profiles of a Li/FEdF/NMC811 cell at selected cycles. c) The evolution of discharge specific capacity and CE of Cu/NMC811 cells employing bare Cu foil with no Li metal as the anode. d) Dis-/charge profiles of a Cu/FEdF/NMC811 cell at selected cycles.

and FEdF is 79.44% and 85.24%, respectively, indicating more irreversible reactions occurring during the initial charge of NMC811 in FE than in FEdF. The CE of both cells increases to higher than 99.9% in the second cycle. In the following 150 cycles, the CE of the Li/FE/NMC811 cell continuously decreases to 99.1%. Since the CE of the Li/NMC811 cells is higher than that seen for Li stripping/plating in FE (Figure 3d), its observed decrease (Figure 4c) indicates continuous (even accelerating) side reactions occurring at the NMC811 electrode side. This is also accompanied by an increase in the average cell polarization from 0.258 V at the 50<sup>th</sup> cycle to 0.466 V at the 200<sup>th</sup> cycle as shown in Figure S8 (Supporting Information) as well as the fast capacity fading. When FEdF is employed as the electrolyte, the Li/NMC811 cells show much higher CE and lower cell polarization. The average CE from the 4<sup>th</sup> to 500<sup>th</sup> cycle is 99.94%, and the CE at the 100<sup>th</sup> and 500<sup>th</sup> cycle is 99.96% and 99.92%, respectively. Furthermore, the cell polarization increases only marginally from 0.167 V at the 50<sup>th</sup> cycle to 0.187 V at the 200<sup>th</sup> cycle. Therefore, the addition of dFBN to FE significantly promotes the reversibility of the NMC811 cathodes. Since the same electrodes were used for the measurements, the improved reversibility fundamentally originates from the interaction between the cathode and the electrolyte, i.e., the formed cathode/electrolyte interphase (CEI).<sup>[7,13,24,37,52]</sup>

In a further step, cells coupling NMC811 cathodes ( $10 \text{ mg cm}^{-2}$ ) and LMAs with a low areal capacity of  $2 \text{ mAh cm}^{-2}$  were assembled, exhibiting a negative to positive areal capacity (N/P) ratio  $\approx 1:1$ . The electrolyte added to each cell was decreased

from the previous 75 to  $20 \mu\text{L}$ , leading to a relatively lean electrolyte condition ( $8.8 \text{ mL Ah}^{-1}$ ). The results of the cycling tests are summarized in Figure 5a. The dis-/charge profiles of the cells employing FEdF and FE as electrolytes at a few selected cycles are shown in Figures 5b and Figure S9 (Supporting Information), respectively. Due to the reduced areal capacity of LMAs, the earlier depletion of lithium metal results in a faster capacity fading of the Li/FEdF/NMC811 cell. Nonetheless, it still exhibits excellent cyclability. Specifically, 162 and  $140 \text{ mAh g}^{-1}$  were obtained at the 200<sup>th</sup> and 250<sup>th</sup> cycle, equaling 88% and 76% retention of the peak capacity ( $184 \text{ mAh g}^{-1}$  at the 50<sup>th</sup> cycle). The remarkable cyclability is a result of the high compatibility of FEdF toward both LMAs and NMC811 cathodes. The resulting specific energy based on the estimated (anode + cathode) active materials weight in a realistic cell is calculated to be  $733 \text{ Wh kg}^{-1}$  at 0.1 C, and  $655 \text{ Wh kg}^{-1}$  at the elevated current rate (Figure S10, Supporting Information). For the Li/FE/NMC811 cells, the reduced areal capacity of LMAs does not severely accelerate the capacity fading. The capacity at the 250<sup>th</sup> cycle is  $40 \text{ mAh g}^{-1}$ , which is very close to the one delivered by the cell with thick lithium foil. Therefore, the fast capacity fading of Li/FE/NMC811 cells is not caused by the depletion of LMA, but, as discussed above, mainly induced by the poor reversibility of the cathode in FE.

Replacing the lithium metal anode with bare Cu foils, we also assembled anode-free Cu/NMC811 coin cells with FE and FEdF as electrolytes. The mass loading of NMC811 and the electrolyte amount added to each cell is still  $10 \text{ mg cm}^{-2}$  and  $20 \mu\text{L}$ ,

respectively. The capacity and CE upon cycling are displayed in Figure 5c. The dis-/charge profiles at representative cycles are shown in Figure 5d and Figure S11 (Supporting Information). At the 100th cycle, the cell employing FEdF exhibits a capacity of  $107 \text{ mAh g}^{-1}$  corresponding to a capacity retention of 62%, while the cell employing FE reaches the same capacity in only 26 cycles. Such improved cycle life is expected due to the higher CE of lithium stripping/plating processes in FEdF than in FE, which is the limiting factor for the cycling stability of such anode-free cells.<sup>[53,54]</sup>

#### 2.4. Chemistry at Electrode/Electrolyte Interphases

The previous electrochemical results have demonstrated the undeniable positive effect of dFBn as cosolvent on the interfacial compatibility toward highly reactive LMAs and NMC811 cathodes. Therefore, the chemical characteristics of the SEI on the LMAs and the CEI on the NMC811 cathodes have been investigated.

To explore the influence of dFBn on the SEI,  $1.5 \text{ mAh cm}^{-2}$  Li metal was deposited on Cu foil either in FE or FEdF at

$0.5 \text{ mA cm}^{-2}$ . The surface morphology of the lithium was then investigated via scanning electron microscopy (SEM). As shown in Figure 6a, both nodule-like and dendritic lithium can be identified in the sample deposited in FE. The lithium dendrites are present throughout the deposited porous lithium layer as shown in Figure S12a (Supporting Information). The surface and cross-section micrographs of the lithium deposited in FEdF are shown in Figure 6b and Figure S12b (Supporting Information), respectively. Without any lithium dendrite, the deposited lithium layer consists of compact nodule-like lithium particles with larger sizes than those in FE. Such a dendrite-free morphology is also observed for the LMA after 100 cycles of stripping/plating in FEdF, as shown in Figure S13 (Supporting Information). Due to the early failure caused by a short circuit of the Li/FE/Li cell (Figure 3c), the morphology of LMAs cycled in FE is not available. Besides the lithium dendrite formation posing a risk of short circuit, the small lithium particles offer increased contact area with the electrolyte, leading to more extensive side reactions and, consequently, inferior lithium plating/stripping CE as well as limited cyclability in FE.

In the next step, X-ray photoelectron spectroscopy (XPS) measurements were carried out on the lithium metal deposited

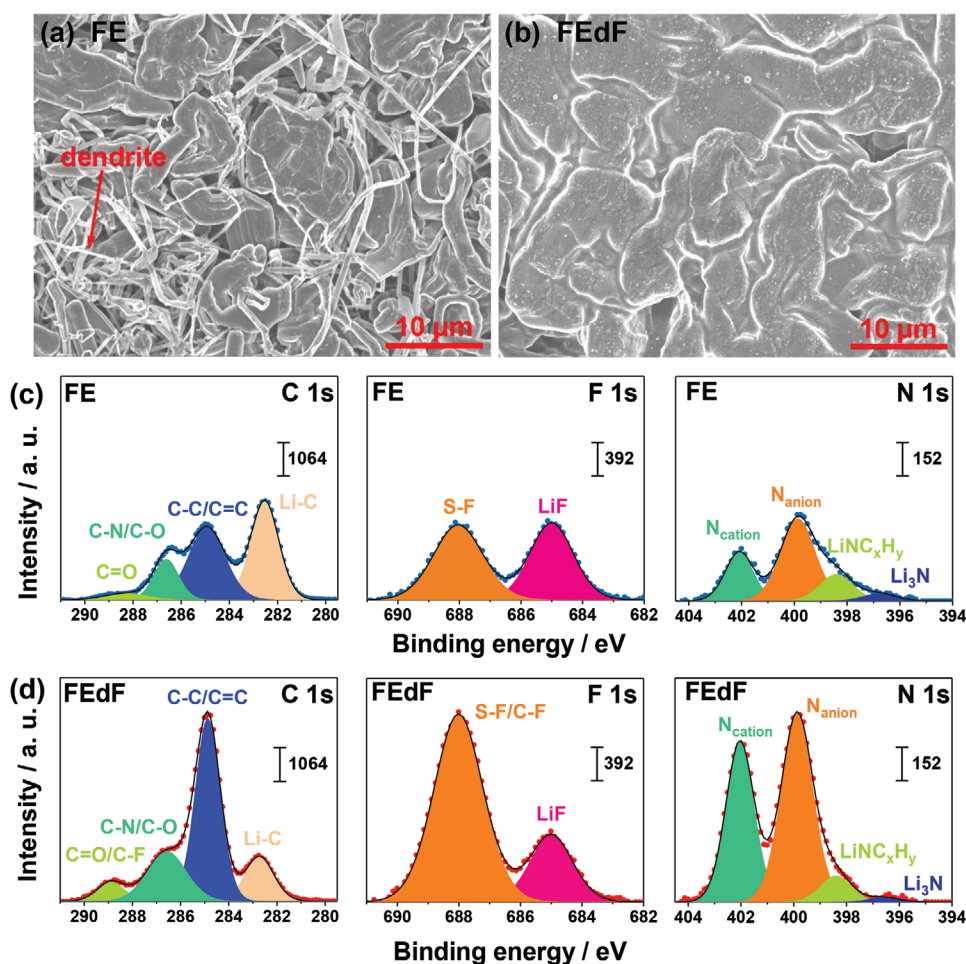


**Figure 6.** Characterization of lithium metal ( $1.5 \text{ mAh cm}^{-2}$ ) deposited in the two electrolytes at  $0.5 \text{ mA cm}^{-2}$ . The SEM images of the surface morphology of the lithium deposited in a) FE and b) FEdF. XPS detail spectra in the C 1s, F 1s, and N 1s regions for the lithium deposited in c) FE and d) FEdF, respectively.

on Cu. The XPS spectra of the FE sample are displayed in Figure 6c. In principle, only Emim<sup>+</sup> contains carbon atoms among the components of FE; hence, the species observed in the C 1s spectra mainly originate from the decomposition of Emim<sup>+</sup>. The peak  $\approx 248.8$  eV is associated with C–C/C=C species in either sp<sup>3</sup> or sp<sup>2</sup> hybridization, both of which exist in Emim<sup>+</sup> and are difficult to be well separated here. Reduction of Emim<sup>+</sup> gives rise to Li–C species, e.g., LiCH<sub>3</sub> and Li<sub>2</sub>C<sub>2</sub> ( $\approx 282.5$  eV),<sup>[49,55]</sup> which is identical to the previous investigation of chemical reduction of imidazolium-based organic cations.<sup>[56,57]</sup> The signal of C–N overlaps with that of C–O, contributing to the peak  $\approx 286.6$  eV.<sup>[56,57]</sup> Another peak at 288.3 eV is assigned to the C = O species.<sup>[58]</sup> In the F 1s spectra, the two peaks located at 685.0 and 688.0 eV are assigned to LiF and to S–F bonds,<sup>[14]</sup> respectively. The LiF clearly results from the decomposition of FSI<sup>−</sup> as it is the only fluorine source in FE. Unlike the spectra in the C 1s and F 1s region, the N 1s spectra include the signals from both Emim<sup>+</sup> and FSI<sup>−</sup>. The peaks at 402.1 and 399.9 eV represent positively charged nitrogen atoms ( $N_{\text{cation}}$ ) from Emim<sup>+</sup> and negatively charged nitrogen atoms ( $N_{\text{anion}}$ ) from FSI<sup>−</sup>, respectively.<sup>[56,57]</sup> The peak at 398.4 eV reflects a chain-like LiNC<sub>x</sub>H<sub>y</sub> forming via further decomposition of  $N_{\text{cation}}$ .<sup>[57]</sup> Furthermore, the minor peak at 396.7 eV is assigned to Li<sub>3</sub>N forming via complete reduction of the N-related species.<sup>[59]</sup> These results demonstrate that both Emim<sup>+</sup> and FSI<sup>−</sup> play a role in the SEI formation on LMAs.

Figure 6d displays the XPS spectra of the lithium layer deposited in FEdF. Since the same anion and organic cation are used in FE and FEdF, the composition of the SEI forming on the deposited Li is very similar. All the signals seen in Figure 6c are also observed in Figure 6d. Meanwhile, the presence of dFBn in FEdF brings some changes in the concentration of some species. Compared with that in Figure 6c, the peak representing C–C/C=C species in C 1s spectra of Figure 6d shows much higher intensity, implying the decomposition of dFBn. The peak which was assigned for the FE electrolytes to C=O species shifts to a higher binding energy  $\approx 288.9$  eV. This shift could at least in part be caused by an overlap with the signal of C–F bonds from dFBn decomposition, which is expected to appear in the range between 288 and 289 eV.<sup>[42]</sup> In the F 1s region, due to the relatively low content of the C–F species and their similar binding energy to that of the F–S bond, the C–F signal cannot be separated from that of S–F.<sup>[42]</sup> Apart from the decomposition of dFBn, an increased contribution of Emim<sup>+</sup> and FSI<sup>−</sup> to the SEI formation in FEdF than that in FE is evidenced by the higher intensities of the S–F (F 1s),  $N_{\text{cation}}$  (N 1s), and  $N_{\text{anion}}$  (N 1s) signals. In contrast, the intensity of the peaks originating from the fully reduced species, e.g., Li–C (C 1s) and LiF (F 1s), is lower in the XPS spectra of the FEdF-based sample, which can be attributed to a thicker SEI weakening the effect of reductive Li metal in FEdF.

In general, dFBn not only takes part in the formation of the SEI but also increases the concentration of the decomposition products of FSI<sup>−</sup> and Emim<sup>+</sup>, leading to a thicker SEI on the surface of the Li deposited in FEdF than in FE. Although the SEI is derived from the electrochemical decomposition of electrolyte or/and chemical reaction between lithium metal and the electrolyte, a thicker SEI does not necessarily mean more electrolyte decomposition in FEdF than in FE, because the lithium

deposited in FEdF exhibits a much larger size. As a matter of fact, the CE of the lithium stripping/plating process in the initial cycle and the following cycles with FEdF is always higher than with FE (as shown in Figure 3e and Table S1, Supporting Information). Therefore, the thick SEI in FEdF is even beneficial for the protection of the highly reactive lithium metal from contact with the electrolyte and consequent side reactions.

Next, the NMC811 electrodes after 100 cycles in either FE or FEdF were investigated. The surface SEM micrographs of NMC811 electrodes in the pristine state, after cycling in FE, and after cycling in FEdF are shown in Figure 7a–c, respectively. Compared with the pristine NMC811, the cycled NMC811 is covered by compact spheres. Furthermore, the spheres on NMC811 cycled in FE is apparently larger than those in FEdF. The cross-sectional micrographs obtained via focused ion-beam (FIB) milling and polishing reveal that in contrast to the bare particle in the pristine electrode (Figure 7d), the NMC811 cycled in FE (Figure 7e) and FEdF (Figure 7f) is obviously covered by an additional layer, which is identical to the spheres observed from the surface micrographs. The thickness of such layer formed in FE and FEdF was determined to be  $\approx 1$   $\mu\text{m}$  and 180 nm, respectively. EDX mapping toward the cross-section of the NMC811 particles in the cycled electrode reveals that these layers are rich in fluorine (insets in Figure 7e,f) and poor in nickel (Figures S14 and S15, Supporting Information), which demonstrates their CEI nature. Since the CEI is generated through irreversible oxidation of the electrolyte, the thicker CEI in FE fits the observed lower CE of NMC811 in FE with respect to those of FEdF (Figure 4c). The ultra-thick CEI blocking the Li<sup>+</sup> migration is thus responsible for the poor cyclability of the NMC811 cathode in FE.

The XPS spectra of the electrodes cycled in FE and FEdF are displayed in Figure 7g,h, respectively. In general, the composition of these two CEIs is very similar. Since the CEI and SEI are generated from the decomposition of the same compounds, some of the components making up the SEI on LMAs (Figure 6c,d) are also observed in the CEIs, e.g., C–N/C–O (C 1s), C–C/C=C (C 1s), S–F (F 1s), LiF (F 1s),  $N_{\text{cation}}$  (N 1s), and  $N_{\text{anion}}$  (N 1s). Meanwhile, some of the deeply reduced species are not observed, e.g., Li–C (C 1s), LiNC<sub>x</sub>H<sub>y</sub> (N 1s), and Li<sub>3</sub>N (N 1s), because the CEI forms mainly via the oxidative decomposition of the electrolytes. Due to the further oxidation of Emim<sup>+</sup> or its decomposition products, O–C=O from the alkyl carbonates is observed at 290.0 eV in the C 1s spectra of Figure 7g.<sup>[58]</sup> It should be noted that this signal might be overlapping with the CF<sub>2</sub> signal of the PVdF binder (expected at  $\approx 290.5$  eV in the C 1s region) of the FEdF sample (Figure 7h);<sup>[58]</sup> the CH<sub>2</sub> groups of PVdF contribute to the C–N/C–O peak (expected at  $\approx 286.5$  eV). The absence of the CF<sub>2</sub> peak from PVdF in the C 1s spectra of FE sample can be explained by the much thicker CEI, which covers the electrode material (including the binder) (Figure 7e).

Despite the similar composition, the concentration of some components is very different. Most importantly, the  $N_{\text{cation}}$  and  $N_{\text{anion}}$  peaks in the N 1s spectra have lower intensity for the FEdF sample (Figure 7h) than for the FE sample (Figure 7g), demonstrating fewer deposition and decomposition of both Emim<sup>+</sup> and FSI<sup>−</sup> in FEdF. Furthermore, the addition of dFBn to the electrolyte significantly increases the intensity

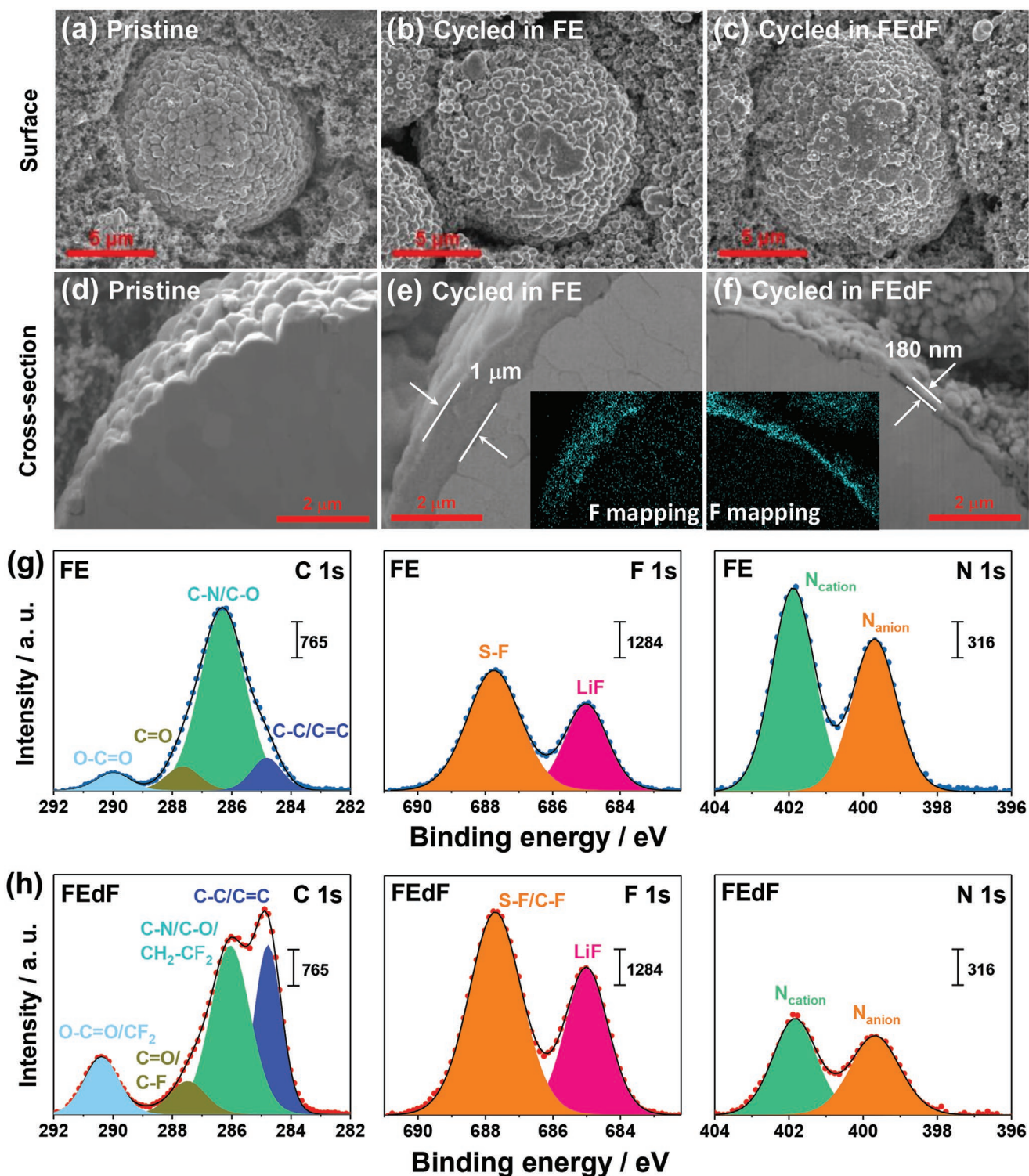


**Figure 7.** Characterization of the NMC811 electrodes. The a–c) surface and d–f) cross-sectional morphology of NMC811 particles in the electrodes (a,d) at pristine state, and after 100 cycles in (b,e) FE and c,f) FEdF, respectively. The insets in (e) and (f) display the corresponding EDX elemental mapping images of fluorine. XPS detail spectra in the C 1s, F 1s, and N 1s regions were recorded for the cycled cathodes after 100 cycles in g) FE and h) FEdF, respectively.

of the C–C/C=C peak and leads to the presence of C–F peak at 288.8 eV in the C 1s spectra, indicating the involvement of dFBn in the CEI formation. Although fewer FSI<sup>-</sup> ions

contribute to the CEI formation in FEdF than in FE, the LiF peak (F 1s) in Figure 7h shows a much higher intensity than that in Figure 7g. This implies that dFBn, the other fluorine-containing

component in FeDF, could also contribute to the formation of LiF, which in turn has been demonstrated to be a good electronic insulator blocking electron leakage and further electrolyte decomposition.

Therefore, the addition of dFBn to the neat IL electrolyte decreases the amount of Emim<sup>+</sup> and FSI<sup>-</sup> deposition and decomposition possibly via formation of LiF, which leads to a more stable CEI exhibiting less thickening upon cycling and consequently high cyclability of NMC811 in FeDF. The EEIs' composition affects the rate of performance and particularly determines the cyclability of batteries, is highly associated with the thermal dynamic properties of the electrolytes.<sup>[60,61]</sup> The investigation on the EEIs clearly demonstrated the involvement of dFBn cosolvent, implying its role in affecting the thermodynamic properties of the electrolytes, which deserves further investigation in the future.

### 3. Conclusions

A dFBn-based LCILE enabling dendrite-free cycling of LMAs with high CE and highly stable cycling of Li/NMC811 cells even with a low N/P ratio has been developed. Poorly coordinating with Li<sup>+</sup> but interacting with Emim<sup>+</sup> via  $\pi$ - $\pi$  stacking, dFBn effectively reduces the viscosity and promotes the Li<sup>+</sup> transport ability of the neat ILE. Although dFBn is barely involved in the Li<sup>+</sup> solvation sheath, it is definitely involved in the formation and affects the chemical composition of the interphases on both the anode and the cathode. On the LMAs, the SEI formed in FeDF consists of more decomposition products of Emim<sup>+</sup> and FSI<sup>-</sup> and is thicker than that in FE, which protects LMAs against side reactions with the electrolyte and therefore promotes their reversibility. On the cathode side, the preferential decomposition of dFBn limits the decomposition of Emim<sup>+</sup> and FSI<sup>-</sup> possibly via the formation of LiF, leading to a thinner but more stable CEI, which promotes better cyclability of NMC811 in FeDF.

### 4. Experimental Section

**Materials:** Molecular sieves (3 Å, Alfa Aesar) were activated at 300 °C under a vacuum (10<sup>-3</sup> mbar) for more than 1 week. 1,2-difluorobenzene (99%, Apollo Scientific Ltd) and DMC (Battery grade, UBE) were dried over the activated molecular sieves for 3 days. LiFSI (99%, PROVISCO CS) was dried at 110 °C under vacuum (10<sup>-3</sup> mbar) for 24 h. EmimFSI (99.5%, Solvionic) was dried at a stepwise increased temperature (room temperature to 60 °C) under a vacuum ( $\approx$ 10<sup>-7</sup> mbar) for 3 days. Lithium metal foils (thickness 500  $\mu$ m, 99.9%, Honjo Metal Co., LTD) were used as received. Polyethylene (PE) separators (SV718 from Asahi Kasei) and surfactant-coated polypropylene (PP) separators (Celgard 3501) were dried at 40 °C under a vacuum (10<sup>-3</sup> mbar) for 24 h. Glass fiber separators (Whatman GF/D) were dried at 150 °C under vacuum (10<sup>-3</sup> mbar) for 24 h.

**Electrolyte and Electrode Preparation and Electrochemical Measurements:** All the electrolyte preparation and cell assembly/disassembly were carried out in an Ar-filled glove box with H<sub>2</sub>O and O<sub>2</sub> levels  $\leq$ 0.1 ppm. The neat ILE (FE) was prepared by dissolving dry LiFSI in dry EmimFSI. The mixture was further dried at 60 °C in a vacuum ( $\approx$ 10<sup>-7</sup> mbar) for 3 days. The FeDF was prepared by diluting the dried FE with a calculated amount of the pre-dried 1,2-difluorobenzene. The NMC811 electrode tapes with Al as a current collector were purchased from Targray, consisting 90 wt.% NMC811, 5 wt.% PVDF binder, and 5 wt.% Super P.

The mass loading of NMC811 is 10 mg cm<sup>-2</sup>. The NMC811 tapes were cut to disk electrodes (diameter: 12 mm) and then dried at 110 °C under vacuum (10<sup>-3</sup> mbar) for 12 h.

CR2032-type coin cells were assembled to evaluate the electrochemical performance of LMAs. If not mentioned otherwise, 14 mm Li discs were used as counter electrodes and 75  $\mu$ L electrolyte was added to each cell. PE separators were used for the cells employing the FeDF electrolyte, while surfactant-coated PP separators were used for the cells employing the FE electrolyte, due to the poor wettability of neat ILEs toward polyolefin separators. For Li/Li, Li/Cu, and Li/NMC811 cells, lithium discs (diameter: 14 mm), Cu foils (diameter: 19 mm), and NMC811 electrodes (diameter: 12 mm) were used as the working electrodes, respectively. For the Li/NMC811 cells with a thin lithium layer, pre-deposited lithium (2 mAh cm<sup>-2</sup> at 0.5 mA cm<sup>-2</sup>) on Cu disks (diameter: 16 mm) was used as the negative electrode, and 20  $\mu$ L electrolyte was added to each cell. For anode-free Cu/NMC811 cells, a bare Cu foil (diameter: 16 mm) was used as a negative electrode, and 20  $\mu$ L electrolyte was added to each cell. For the evaluation of anodic corrosion of the Al current collector, three-electrode Swagelok T-cells employing lithium metal discs as counter and reference electrodes, respectively, were assembled using GF/D separators, and 100  $\mu$ L electrolyte was added to each cell. Bare Al foils were used as the working electrodes.

All the electrochemical measurements were carried out at 20 °C. The galvanostatic measurements were performed with a battery cycler (Maccor series 4000). CV measurements were performed with a galvanostat/potentiostat VMP (Bio-Logic).

**Characterization:** The samples for NMR measurements were prepared in the dry room with a dew point < -70 °C. FE and FeDF were transferred to 5 mm NMR tubes, hosting a sealed capillary containing deuterated dimethylsulfoxide (DMSO-d<sub>6</sub>) used as a lock and chemical shift reference, and immediately flame-sealed. NMR measurements were performed at 293 K without sample spinning on a Bruker NEO 500 console (11.74 T) equipped with a direct observe BBFO (broadband including fluorine) iProbe and a variable-temperature unit. The instrument was carefully tuned, shimmed, and the 90° pulses calibrated. <sup>1</sup>H, <sup>19</sup>F, and <sup>7</sup>Li self-diffusion experiments were performed using the bipolar pulse longitudinal eddy current delay (BPP-LED) pulse sequence by applying sine-shaped pulsed magnetic field gradients along the z-direction up to a maximum strength of G = 53.5 G cm<sup>-1</sup>. The conductivity of the electrolytes was determined via electrochemical impedance spectroscopy by an integrated liquid conductivity system MCS 10 (Material Mates-Biologic), using sealed high-temperature conductivity cells (HTCC, Material Mates) with Pt-black electrodes. The conductivity values averaged over 60 min ( $\approx$ 60 data points) were used. The cell constants were determined using a 0.01 M KCl standard solution. The electrolyte viscosity was measured in a dry room environment utilizing an Anton-Paar MCR 102 rheometer, applying a constant shear rate of 10 s<sup>-1</sup> and using a Peltier system for temperature control. The viscosity values averaged over 2.5 min (50 data points) were used. The Raman measurements were recorded with a RAM II FT-Raman module of a Bruker Vertex70v FT-IR spectrometer with a laser wavelength of 1064 nm and laser power of 300 mW. Scanning electron microscopy (SEM) images were obtained using a Zeiss CrossBeam XB340 microscope equipped with an energy dispersive X-ray (EDX) detector. To investigate the internal structure of the electrode and active material particles, cross-sections were prepared on a Capella focused ion-beam (FIB, gallium ion source) system using milling and polishing currents of 30 and 3 nA at an acceleration voltage of 30 kV, respectively. All samples recovered from cycled cells were transferred to the microscope under an argon atmosphere using an air-tight transfer box (Sample Transfer Shuttle, SEMILAB). Micrographs were acquired from the top and in cross-sectional configuration (under a tilt-angle of 54°) after FIB preparation using smart SEM software for tilt correction to compensate for the image distortion due to the tilt of 54° to the optical axis. XPS measurements were carried out in an ultrahigh vacuum surface analysis system (10<sup>-10</sup> mbar) with a Phoibos 150 XPS spectrometer (Specs – Surface Concept) equipped with a delay line detector. Monochromatized Al K $\alpha$  radiation (200 W) was used for the measurements and the scans

were acquired at 30 eV pass energy at the analyzer for detailed scans. The peak fitting was carried out by CasaXPS software, using Shirley-type backgrounds and 70% Gaussian – 30% Lorentzian peak profile functions. For the postmortem characterization, the electrodes were removed from the cells and washed with the dried DMC in the Ar-filled glove box. The samples were transferred in sealed boxes from the glove box to the SEM and XPS instruments to prevent exposure to humid air.

**MD Simulation:** Molecular dynamics simulations were carried out using Amber 18 software<sup>[62]</sup> exploiting the GAFF force field.<sup>[63]</sup> The atomic partial charges were obtained with the RESP algorithm from DFT calculations run with Gaussian09e at the B3LYP/6-311++G\*\* level of theory.<sup>[64]</sup> The starting random molecular arrangements were obtained by Packmol.<sup>[65]</sup> The simulation went through different steps, starting from a geometrical relaxation, followed by gradual heating of the system from 0 to 50 K in several NVT sessions. The systems were then equilibrated at 300 K for 20 ns in NPT ensemble, and for a further 20 ns in the NVT. A final productive NVT phase of 10 ns was then used for the analysis. For the productive phase, the time step used was 2 fs, and the simulation was dumped every 1000 steps, obtaining a final trajectory of 5000 frames spaced by 2ps each. In order to account for charge transfer and polarization effects, the atomic charges of the ionic species were scaled by a factor of 0.74, which is known to yield reliable results for ionic liquids.<sup>[66]</sup> The trajectories were analyzed with Travis.<sup>[67,68]</sup>

## Supporting Information

Supporting Information is available from the Wiley Online Library or from the author.

## Acknowledgements

This work was supported by the China Scholarship Council (CSC); the German Federal Ministry of Education and Research (BMBF) within the LILLINT (03XP0225D) project; the Helmholtz Association Basic funding; and the postdoctoral fellowship in the framework of the “MSCA EF Master Class 2018” funding programme in the Politecnico di Milano.

Open access funding enabled and organized by Projekt DEAL.

## Conflict of Interest

The authors declare no conflict of interest.

## Author Contributions

X.L. performed conceptualization, electrochemical tests, and wrote the original draft. A.M. performed MD simulation, and reviewed and edited the final manuscript. T.D. performed XPS measurements, and reviewed and edited the final manuscript. M.E.D.P. performed NMR measurements, and reviewed and edited the final manuscript. X.D. performed tests for physicochemical properties, and reviewed and edited the final manuscript. M.K. performed SEM-FIB tests, and reviewed and edited the final manuscript. A.M. performed NMR measurements, and reviewed and edited the final manuscript. S.P. supervised the study, acquired funding, and reviewed and edited the final manuscript.

## Data Availability Statement

The data that support the findings of this study are available on request from the corresponding author. The data are not publicly available due to privacy or ethical restrictions.

## Keywords

1, 2-difluorobenzene, ionic liquids, lithium metal batteries, locally concentrated electrolytes, nickel-rich cathodes

Received: March 12, 2022

Revised: April 16, 2022

Published online: May 18, 2022

- [1] G. M. Hobold, J. Lopez, R. Guo, N. Minafra, A. Banerjee, Y. Shirley Meng, Y. Shao-Horn, B. M. Gallant, *Nat. Energy* **2021**, 6, 951.
- [2] W. Li, E. M. Erickson, A. Manthiram, *Nat. Energy* **2020**, 5, 26.
- [3] W. Xue, M. Huang, Y. Li, Y. G. Zhu, R. Gao, X. Xiao, W. Zhang, S. Li, G. Xu, Y. Yu, P. Li, J. Lopez, D. Yu, Y. Dong, W. Fan, Z. Shi, R. Xiong, C. J. Sun, I. Hwang, W. K. Lee, Y. Shao-Horn, J. A. Johnson, J. Li, *Nat. Energy* **2021**, 6, 495.
- [4] X. Fan, C. Wang, *Chem. Soc. Rev.* **2021**, 50, 10486.
- [5] C. Niu, D. Liu, J. A. Lochala, C. S. Anderson, X. Cao, M. E. Gross, W. Xu, J. G. Zhang, M. S. Whittingham, J. Xiao, J. Liu, *Nat. Energy* **2021**, 6, 723.
- [6] G. L. Xu, X. Liu, A. Daali, R. Amine, Z. Chen, K. Amine, *Adv. Funct. Mater.* **2020**, 30, 2004748.
- [7] X. Zhang, L. Zou, Z. Cui, H. Jia, M. H. Engelhard, B. E. Matthews, X. Cao, Q. Xie, C. Wang, A. Manthiram, J. G. Zhang, W. Xu, *Mater. Today* **2021**, 44, 15.
- [8] X. Cao, X. Ren, L. Zou, M. H. Engelhard, W. Huang, H. Wang, B. E. Matthews, H. Lee, C. Niu, B. W. Arey, Y. Cui, C. Wang, J. Xiao, J. Liu, W. Xu, J. G. Zhang, *Nat. Energy* **2019**, 4, 796.
- [9] T. Li, X. Q. Zhang, P. Shi, Q. Zhang, *Joule* **2019**, 3, 2647.
- [10] J. Chen, Z. Li, N. Sun, J. Xu, Q. Li, X. Yao, J. Ming, Z. Peng, *ACS Energy Lett.* **2022**, 7, 1594.
- [11] J. Li, L. E. Downie, L. Ma, W. Qiu, J. R. Dahn, *J. Electrochem. Soc.* **2015**, 162, A1401.
- [12] H. H. Ryu, K. J. Park, C. S. Yoon, Y. K. Sun, *Chem. Mater.* **2018**, 30, 1155.
- [13] X. Fan, L. Chen, O. Borodin, X. Ji, J. Chen, S. Hou, T. Deng, J. Zheng, C. Yang, S. C. Liou, K. Amine, K. Xu, C. Wang, *Nat. Nanotechnol.* **2018**, 13, 715.
- [14] X. Fan, L. Chen, X. Ji, T. Deng, S. Hou, J. Chen, J. Zheng, F. Wang, J. Jiang, K. Xu, C. Wang, *Chem* **2018**, 4, 174.
- [15] J. Zheng, Y. Yang, X. Fan, G. Ji, X. Ji, H. Wang, S. Hou, M. R. Zachariah, C. Wang, *Energy Environ. Sci.* **2019**, 12, 615.
- [16] J. Fu, X. Ji, J. Chen, L. Chen, X. Fan, D. Mu, C. Wang, *Angew. Chemie – Int. Ed.* **2020**, 59, 22194.
- [17] Z. Yu, H. Wang, X. Kong, W. Huang, Y. Tsao, D. G. Mackanic, K. Wang, X. Wang, W. Huang, S. Choudhury, Y. Zheng, C. V. Amanchukwu, S. T. Hung, Y. Ma, E. G. Lomeli, J. Qin, Y. Cui, Z. Bao, *Nat. Energy* **2020**, 5, 526.
- [18] M. A. Philip, R. T. Haasch, J. Kim, J. Yang, R. Yang, I. R. Kochetkov, L. F. Nazar, A. A. Gewirth, *Batter. Supercaps* **2021**, 4, 294.
- [19] H. Wang, Z. Yu, X. Kong, W. Huang, Z. Zhang, D. G. Mackanic, X. Huang, J. Qin, Z. Bao, Y. Cui, *Adv. Mater.* **2021**, 33, 2008619.
- [20] Y. Zhang, T. T. Zuo, J. Popovic, K. Lim, Y. X. Yin, J. Maier, Y. G. Guo, *Mater. Today* **2020**, 33, 56.
- [21] A. Heist, S.-H. Lee, *J. Electrochem. Soc.* **2019**, 166, A1677.
- [22] A. Heist, S. Hafner, S.-H. Lee, *J. Electrochem. Soc.* **2019**, 166, A873.
- [23] H. Sun, G. Zhu, Y. Zhu, M. C. Lin, H. Chen, Y. Y. Li, W. H. Hung, B. Zhou, X. Wang, Y. Bai, M. Gu, C. L. Huang, H. C. Tai, X. Xu, M. Angell, J. J. Shyue, H. Dai, *Adv. Mater.* **2020**, 32, 2001741.
- [24] F. Wu, S. Fang, M. Kuenzel, A. Mullaliu, J. K. Kim, X. Gao, T. Diemant, G. T. Kim, S. Passerini, *Joule* **2021**, 5, 2177.
- [25] U. Pal, F. Chen, D. Gyabang, T. Pathirana, B. Roy, R. Kerr, D. R. MacFarlane, M. Armand, P. C. Howlett, M. Forsyth, *J. Mater. Chem. A* **2020**, 8, 18826.

- [26] R. S. Kühnel, N. Böckenfeld, S. Passerini, M. Winter, A. Balducci, *Electrochim. Acta* **2011**, *56*, 4092.
- [27] Q. J. Meisner, T. Rojas, T. Glossmann, A. Hintennach, Q. Liu, J. Cao, P. C. Redfern, A. T. Ngo, L. A. Curtiss, Z. Zhang, *J. Electrochem. Soc.* **2020**, *167*, 070528.
- [28] U. Pal, D. Rakov, B. Lu, B. Sayahpour, F. Chen, B. Roy, D. R. MacFarlane, M. Armand, P. C. Howlett, Y. S. Meng, M. Forsyth, *Energy Environ. Sci.* **2022**, <https://doi.org/10.1039/D1EE02929K>.
- [29] X. Liu, M. Zarrabeitia, A. Mariani, X. Gao, H. M. Schütz, S. Fang, T. Bizien, G. A. Elia, S. Passerini, *Small Methods* **2021**, *5*, 2100168.
- [30] S. Lee, K. Park, B. Koo, C. Park, M. Jang, H. Lee, H. Lee, *Adv. Funct. Mater.* **2020**, *30*, 2003132.
- [31] Z. Wang, F. Zhang, Y. Sun, L. Zheng, Y. Shen, D. Fu, W. Li, A. Pan, L. Wang, J. Xu, J. Hu, X. Wu, *Adv. Energy Mater.* **2021**, *11*, 2003752.
- [32] X. Liu, A. Mariani, M. Zarrabeitia, M. E. Di Pietro, X. Dong, G. A. Elia, A. Mele, S. Passerini, *Energy Storage Mater.* **2022**, *44*, 370.
- [33] X. Cao, H. Jia, W. Xu, J.-G. Zhang, *J. Electrochem. Soc.* **2021**, *168*, 010522.
- [34] S. Chen, J. Zheng, D. Mei, K. S. Han, M. H. Engelhard, W. Zhao, W. Xu, J. Liu, J. G. Zhang, *Adv. Mater.* **2018**, *30*, 1706102.
- [35] S. Chen, J. Zheng, L. Yu, X. Ren, M. H. Engelhard, C. Niu, H. Lee, W. Xu, J. Xiao, J. Liu, J. G. Zhang, *Joule* **2018**, *2*, 1548.
- [36] N. Piao, X. Ji, H. Xu, X. Fan, L. Chen, S. Liu, M. N. Garaga, S. G. Greenbaum, L. Wang, C. Wang, X. He, *Adv. Energy Mater.* **2020**, *10*, 1903568.
- [37] X. Ren, L. Zou, X. Cao, M. H. Engelhard, W. Liu, S. D. Burton, H. Lee, C. Niu, B. E. Matthews, Z. Zhu, C. Wang, B. W. Arey, J. Xiao, J. Liu, J. G. Zhang, W. Xu, *Joule* **2019**, *3*, 1662.
- [38] G. Zhang, X. Deng, J. Li, J. Wang, G. Shi, Y. Yang, J. Chang, K. Yu, S. Sen Chi, H. Wang, P. Wang, Z. Liu, Y. Gao, Z. Zheng, Y. Deng, C. Wang, *Nano Energy* **2022**, *95*, 107014.
- [39] X. Cao, L. Zou, B. E. Matthews, L. Zhang, X. He, X. Ren, M. H. Engelhard, S. D. Burton, P. Z. El-Khoury, H. S. Lim, C. Niu, H. Lee, C. Wang, B. W. Arey, C. Wang, J. Xiao, J. Liu, W. Xu, J. G. Zhang, *Energy Storage Mater.* **2021**, *34*, 76.
- [40] H. Yoon, P. C. Howlett, A. S. Best, M. Forsyth, D. R. MacFarlane, *J. Electrochem. Soc.* **2013**, *160*, A1629.
- [41] H. Yoon, A. S. Best, M. Forsyth, D. R. MacFarlane, P. C. Howlett, *Phys. Chem. Chem. Phys.* **2015**, *17*, 4656.
- [42] D. J. Yoo, S. Yang, K. J. Kim, J. W. Choi, *Angew. Chemie – Int. Ed.* **2020**, *59*, 14869.
- [43] Z. Jiang, Z. Zeng, X. Liang, L. Yang, W. Hu, C. Zhang, Z. Han, J. Feng, J. Xie, *Adv. Funct. Mater.* **2021**, *31*, 2005991.
- [44] Z. Jiang, Z. Zeng, B. Zhai, X. Li, W. Hu, H. Zhang, S. Cheng, J. Xie, *J. Power Sources* **2021**, *506*, 230086.
- [45] Y. Cai, Q. Zhang, Y. Lu, Z. Hao, Y. Ni, J. Chen, *Angew. Chemie – Int. Ed.* **2021**, *60*, 25973.
- [46] M. Kunze, S. Jeong, E. Paillard, M. Schönhoff, M. Winter, S. Passerini, *Adv. Energy Mater.* **2011**, *1*, 274.
- [47] M. Beran, J. Přihoda, Z. Žák, M. Černík, *Polyhedron* **2006**, *25*, 1292.
- [48] B. D. Adams, J. Zheng, X. Ren, W. Xu, J. G. Zhang, *Adv. Energy Mater.* **2018**, *8*, 1702097.
- [49] X. Ren, S. Chen, H. Lee, D. Mei, M. H. Engelhard, S. D. Burton, W. Zhao, J. Zheng, Q. Li, M. S. Ding, M. Schroeder, J. Alvarado, K. Xu, Y. S. Meng, J. Liu, J. G. Zhang, W. Xu, *Chem* **2018**, *4*, 1877.
- [50] S. Jiao, J. Zheng, Q. Li, X. Li, M. H. Engelhard, R. Cao, J. G. Zhang, W. Xu, *Joule* **2018**, *2*, 110.
- [51] J. Xiao, Q. Li, Y. Bi, M. Cai, B. Dunn, T. Glossmann, J. Liu, T. Osaka, R. Sugiura, B. Wu, J. Yang, J. G. Zhang, M. S. Whittingham, *Nat. Energy* **2020**, *5*, 561.
- [52] T. Deng, X. Fan, L. Cao, J. Chen, S. Hou, X. Ji, L. Chen, S. Li, X. Zhou, E. Hu, D. Su, X. Q. Yang, C. Wang, *Joule* **2019**, *3*, 2550.
- [53] Y. Qiao, H. Yang, Z. Chang, H. Deng, X. Li, H. Zhou, *Nat. Energy* **2021**, *6*, 653.
- [54] T. Pathirana, R. Kerr, M. Forsyth, P. C. Howlett, *Sustain. Energy Fuels* **2021**, *5*, 4141.
- [55] G. F. Meyers, M. B. Hall, J. W. Chinn, R. J. Lagow, *J. Am. Chem. Soc.* **1985**, *107*, 1413.
- [56] M. Olschewski, R. Gustus, O. Höfft, A. Lahiri, F. Endres, *J. Phys. Chem. C* **2017**, *121*, 2675.
- [57] M. Olschewski, R. Gustus, M. Marschewski, O. Höfft, F. Endres, *Phys. Chem. Chem. Phys.* **2014**, *16*, 25969.
- [58] J. F. Moulder, W. F. Stickle, P. E. Sobol, K. D. Bomben, *Handbook of X-ray Photoelectron Spectroscopy*, Perkin-Elmer Corporation, Physical Electronics Division, Minnesota, USA **1995**.
- [59] K. Park, B. C. Yu, J. B. Goodenough, *Adv. Energy Mater.* **2016**, *6*, 1502534.
- [60] Y. Zou, Z. Cao, J. Zhang, W. Wahyudi, Y. Wu, G. Liu, Q. Li, H. Cheng, D. Zhang, G. T. Park, L. Cavallo, T. D. Anthopoulos, L. Wang, Y. K. Sun, J. Ming, *Adv. Mater.* **2021**, *33*, 2102964.
- [61] Q. Li, Z. Cao, W. Wahyudi, G. Liu, G. T. Park, L. Cavallo, T. D. Anthopoulos, L. Wang, Y. K. Sun, H. N. Alshareef, J. Ming, *ACS Energy Lett.* **2021**, *6*, 69.
- [62] D. A. Case, T. E. Cheatham, T. Darden, H. Gohlke, R. Luo, K. M. Merz, A. Onufriev, C. Simmerling, B. Wang, R. J. Woods, *J. Comput. Chem.* **2005**, *26*, 1668.
- [63] J. Wang, R. M. Wolf, J. W. Caldwell, P. A. Kollman, D. A. Case, *J. Comput. Chem.* **2004**, *25*, 1157.
- [64] M. J. Frisch, G. W. Trucks, H. B. Schlegel, G. E. Scuseria, M. A. Robb, J. R. Cheeseman, G. Scalmani, V. Barone, G. A. Petersson, H. Nakatsuji, X. Li, M. Caricato, A. Marenich, J. Bloino, B. G. Janesko, R. Gomperts, B. Mennucci, H. P. Hratchian, J. V. Ort, D. J. Fox, **2009**.
- [65] L. Martinez, R. Andrade, E. G. Birgin, J. M. Martínez, *J. Comput. Chem.* **2009**, *30*, 2157.
- [66] A. Mariani, R. Caminiti, M. Campetella, L. Gontrani, *Phys. Chem. Chem. Phys.* **2016**, *18*, 2297.
- [67] M. Brehm, B. Kirchner, *J. Chem. Inf. Model.* **2011**, *51*, 2007.
- [68] M. Brehm, M. Thomas, S. Gehrke, B. Kirchner, *J. Chem. Phys.* **2020**, *152*, 164105.